Journal of Materials Chemistry A

Accepted Manuscript

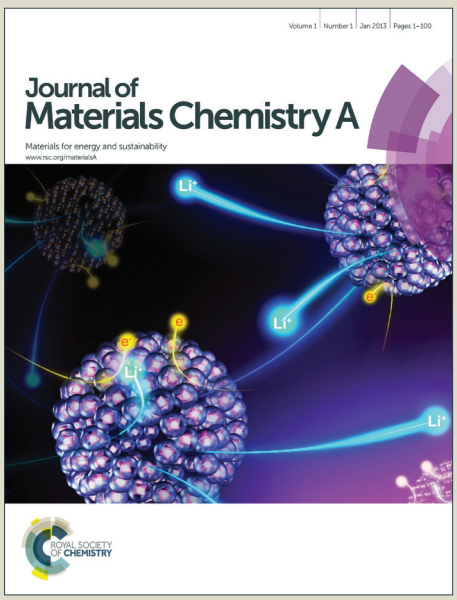

ROYAL SOCIETY OF CHEMISTRY

www.rsc.org/materialsA

Journal Name

RSCPublishing

ARTICLE

Synthesis of Nitrogen and Boron co-doped Carbon (CNB) and Their CO_2 Capture Properties: From Porous to Hollow Granule Structure

Cite this: DOI: 10.1039/x0xx00000x

Received 00th January 2014,
Accepted 00th January 2014

DOI: 10.1039/x0xx00000x

www.rsc.org/

Jinhong Kim, Jisun Han, Daegwon Ha and Shinhoo Kang*

Since its first synthesis, carbide-derived carbon has been examined for use in various applications, and its performance has been both interesting and outstanding. Despite its useful conformal character, its variety of chemical composition is limited because functionalized atoms in its carbonaceous structure, especially with nitrogen, are unstable during high-temperature processing. In this paper, we demonstrate the enhancement of nitrogen stability and an increase in surface area by boron addition. We also synthesized a hollow granule structure of nitrogen/boron co-doped porous carbon in high yield by using a nitrogen-rich precursor without any additive template. High CO_2 capture (3.7 mmol/g) was measured at ambient temperature and 1bar with an excellent CO_2/N_2 selectivity.

Introduction

Carbon is an important second period element. This abundant and inexpensive element exists in zero- to three-dimensional form and has high thermal and chemical stability. It can form materials with a high surface area, and is therefore often used in such as in supporting materials, electrochemical devices, and gas storage materials.[1-3] However, its high stability results in low activity in chemical reactions, limiting its applicability. Carbon structures doped with adjacent nitrogen and/or boron can be potential solution to pure carbon for enhanced reactivity to guest molecules.[4, 5]

Nitrogen-doped porous carbon (CN) materials have maintained extensive research interest. Several methods for their synthesis have been demonstrated, including ammonia heat treatment[6] and copolymerization followed by carbonization.[7] The most popular and effective synthesis method employs templates with suitable nitrogen precursors, e.g., melamine,[8] acetonitrile,[9] and diaminobenzene.[10] Boron-doped porous carbon (CB) has rarely been reported on, because the bonding between carbon and boron is unstable under moderate processing conditions. CB materials require high-temperature synthesis, and few papers have reported the substitution of a small amount of boron into the porous carbon structure to demonstrate the improved gas sorption properties of the doped material.[11, 12]

In recent years, nitrogen-and-boron-co-doped porous carbon (CNB) has received much attention, with examples being verified as phosphors,[13] catalysts,[14, 15] supercapacitors[16, 17] and gas sorption materials.[18] However, these materials usually consist of two separate phases, a C–N- and a B–N-rich phase owing to the C–B instability.[19] Given the difficulty of obtaining a homogenous CNB framework, an effective way of the CNB synthesis is highly sought after.

In this paper, we discuss our breakthrough synthesis of boron-aided nitrogen-doped porous carbon to create CNBs with a robust matrix. The CNB synthesis was by a chlorination method previously discussed for porous boron nitride.[20] This synthetic procedure, which is similar to the carbide-derived carbon (CDC) process,[21] easily produced well-developed pores without requiring any templates. Chlorine gas worked as metal scavenger and metal chloride was removed as a gaseous phase. Small amounts of boron were found to act as a stabilizer for the nitrogen-doped carbon structure at a relatively high temperature of 800°C. We denoted samples as CN-XY and CNB-XY according to whether a boron source was added; XY represents the carbon-to-nitrogen ratio of the $Ti(C_xN_y)$ precursors ($y = 1 - x$).

Furthermore, a hollow granule CN (B) structure, which is generally only prepared by the hard template method,[22, 23] was achieved by using a nitrogen-rich precursor. Though some graphitic C_3N_4-type hollow spheres have been prepared without using hard templates,[24, 25] no reports exist, to the best of our knowledge, for CN (B) with relatively low nitrogen content. Given that the hard template method shows disadvantages, for example it is complex, gives low yields, and produces shells lacking structural robustness,[26, 27] our one-step self-templating method is highly desirable. Despite its moderate surface area, hollow CNB37 (synthesized from the $Ti(C_{0.3}N_{0.7})$ precursor) has a high capacity for CO2 capture. The CO_2/N_2 selectivity, one of the key factors for post-combustion CO_2 capture, is improved significantly. This result might contribute to aid carbon capture and storage technology, and thus might be very useful, considering that there is an urgent requirement for greenhouse gas reduction.[28, 29]

Experimental

Synthesis procedure. CNs were synthesized based on our previous reported method as follows. A quartz boat containing 2 g $Ti(C_xN_y)$ (Treibacher Industry AG) was placed in a quartz tube furnace under flowing argon. The furnace was heated to 800 °C at 10 °C/min, after which the argon was replaced by chlorine and maintained under these conditions for 3 h. After chlorination, argon gas was fed into the system again and the furnace was cooled to 600 °C. Further heat treatment was performed at 600 °C in a hydrogen atmosphere for 2 h to remove residual chlorine trapped in the pores. BCNs were synthesized in the same way but with the addition of a boron precursor. $Ti(C_xN_y)$ and TiB_2 were mixed by hand in a mortar jar for 15 min before the heat treatment was repeated. The mixing molar ratio of carbon to boron in the precursors was 4:1 for all the CNBs. Samples with high boron contents were synthesized by changing mixing ratio of $Ti(C_xN_y)$ and TiB_2 to 1:2 for comparison.

Characterization. N_2 and CO_2 adsorption were measured using a BELSORP-mini (BEL JAPAN INC., Japan) at 298 K. Before the gas adsorption, pre-heat treatment was conducted for 24 h at 300 °C under vacuum to remove residual water and other physically adsorbed impurities. The specific surface area of each sample was determined using the BET equation based on 77 K N_2 adsorption from 0.01 atm to 0.15 atm. The CO_2/N_2 selectivity was obtained using the IAST from the single component gas sorption properties, measured at the same temperature (298 K). The modified IAST was used after fitting using the single-site Langmuir model. Details are provided in the supporting information. X-ray diffraction (XRD) spectra were obtained using a Rigaku X-ray diffractometer (D-MAX2500-PC) with Cu-Kα radiation. XPS was carried out using an ASIS-Hsi (KRATOS, UK) with Mg in Mg/Al dual anode source. A binding energy of 284.5 eV was selected as a reference for C 1s. The bulk boron content was measured by ICP-AES (PerkinElmer Inc., Optima-4300 DV) and C, N, and O were determined by EA (Thermo Scientific, Flash2000). Morphological studies were conducted by FE-SEM (Hitachi, SU70, 5 kV) and TEM was conducted using a Tecnai F20 (FEI, 200 kV). EELS and the corresponding elemental mapping were also conducted using a Tecnai F20.

Density functional theory calculation. The CASTEP code was used to optimize the boron- or nitrogen-doped graphene monolayer. To prevent mutual interaction between the guest atoms, a 9 × 9 layer super-cell (128 atoms) was introduced with a 15 Å vacuum slab. The ultrasoft pseudo-potential with spin-polarized generalized gradient approximation Perdew–Burke–Ernzerhof (GGA-PBE) functional

was used to optimize the geometry. The cut-off energy was set at 330 eV, and the convergence tolerance was 5.0 × 10−6 eV/atom.

Results & Discussion

Figure 1 shows the N_2 adsorption properties of CNs and CNBs at 77K. With the exception of less-porous CN37, all samples have type I and IV pores, which implies the active and simultaneous development of micro- and meso- pores. Boron addition causes a sharp increase in the adsorption at P/P0 = 0.90 − 0.99 with an H2-type hysteresis loop, especially when precursors with high nitrogen contents are used. The results indicate that the size and shape of the pores are not unimodal and that the pore size spreads from the micro- to the macro-pore regions. Detailed textural properties of the samples are summarized in Table S1. No significant textural differences exist between CN73 and CNB73 except for a small change in meso- and macro- pore volume due to the high amount of carbon in the Ti($C_{0.7}N_{0.3}$) precursor.

The results are different for CN55 and CNB55. Given that the nitrogen functional groups are not sufficiently stable during high-temperature chlorination, the CN55 structure collapses partially because of a deficiency in neighboring carbons caused by the formation of CNCl and CxNy gases.[30] Thus, the Brunauer–Emmett–Teller (BET) surface area decreases as pores are encroached in CN55. Pore retention is observed in CNB55 and becomes very obvious when CN37 and CNB37 are compared. Since most of the CN37 structure is lost as gaseous CNCl and C_xN_y,[30] the yield is extremely low (1.5%) and pore formation is also retarded. However, after boron addition, the yield is increased significantly to 18.3% with pore development. The BET surface area also increases significantly from 183 m^2/g to 730 m^2/g. Especially macropores, which results in N_2 adsorption at P/P0 > 0.95, further developed as nitrogen content of precursors increase.

Field emission-scanning electron microscopy (FE-SEM) images in Figure 2 show that the CNB morphology is similar to that of the Ti(C_xN_y) precursors. This observation is consistent with conventional TiC-CDC products, which have a narrow pore size distribution.[21, 31] The increase in nitrogen content in the Ti(C_xN_y) precursors changes their morphologies from an angular to a rounded shape with a decrease in average particle size. Corresponding CNB

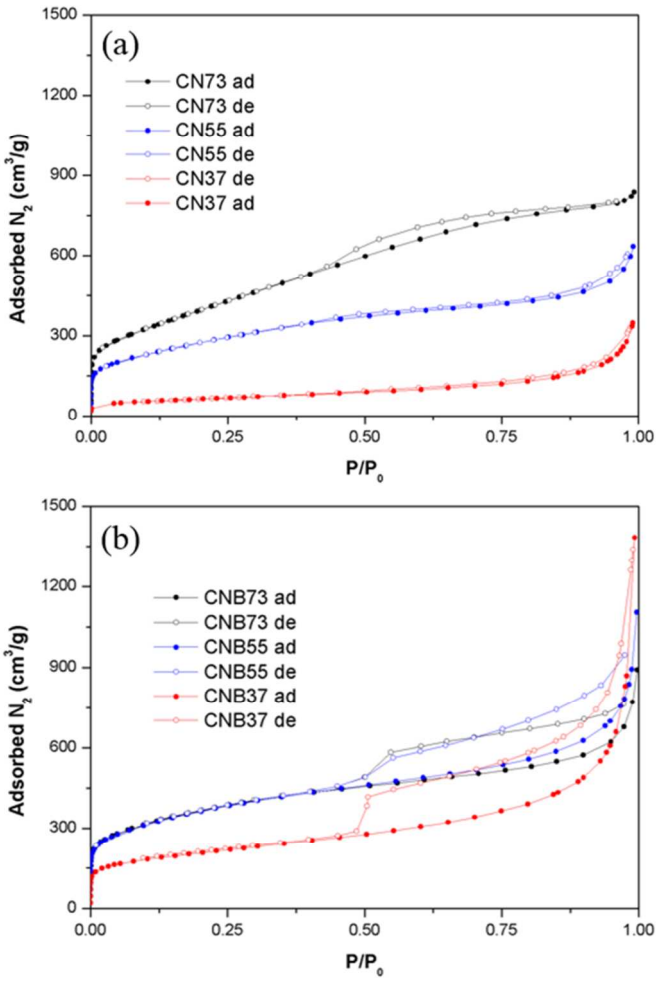

Figure 1. N_2 adsorption (ad, solid) and desorption (de, empty) curves of CNs (a) and CNBs (b) at 77K. Each color indicates CN(B)73 (black), CN(B)55 (blue), CN(B)37 (red) repectively.

granules exhibit conformal-like transformations from the precursors. But a partially broken particle in the inset of Figure 2(f) indicates the hollow nature of the CNB37 granules. Samples were characterized further by transmission electron microscopy (TEM). Figure S1 shows typical turbostratic images for CNB73 and CNB55. Some short-range ordered graphene-like layers, indicated by circles, are detected, especially at the edge boundaries.

TEM images of CN37 and CNB37 are shown in Figure 3. The hollow granule structure of CNB37 (Figure 3(b)) is very different from that of CN37 (Figure 3(a)). The shell thickness is estimated to be approximately 7–8 nm. Two diffusive rings were obtained from the selected-area electron diffraction (SAED) pattern: (100)/(101) and (110)/(112) patterns with 0.21nm and 0.12 nm d-spacing, respectively. The existence of short-range ordered (002) interlayers, which are observed close to the boundaries, confirms the turbostratic

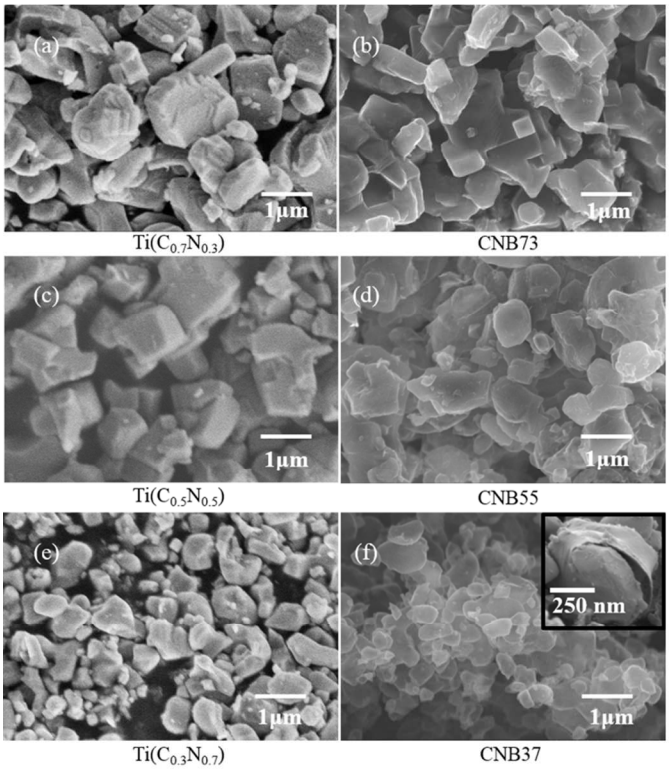

Figure 2. FE-SEM images of $Ti(C_xN_y)$ precursors (left) and their corresponding CNB granules (right). Inset in (f) shows a partially broken CNB granule with empty space inside.

nature of the CNB37 (Figure 3(c), (d)). This character is also supported by two broad peaks with 0.34~0.36 nm interlayer distance of (002) plane in the X-ray diffraction spectrum as shown in Figure S2. Although hollow carbon [32, 33] and boron nitrides (BN)[34] granule structures without a hard template have been reported, hollow CN or CNB structures have rarely been mentioned. This is because C–N bonds less stable than C–C or B–N bonds, and tend to decompose easily, resulting in the collapse of the structure during synthesis.

The mechanism for the formation of hollow CNB is shown in Scheme 1. For simplicity, the $Ti(C_{0.3}N_{0.7})$ precursor is drawn to be spherical. Based on the TiC-CDC formation, the initial morphology is expected to be conformal to that of $Ti(C_{0.3}N_{0.7})$ after titanium extraction by chlorination, resulting in an analogous porous structure as shown in Figure 2(f). CNB37 of high stability is believed to form along the surfaces of the $Ti(C_{0.3}N_{0.7})$ particles as shown in Figure 2(e), which is in contact with TiB_2 precursors. This is in contrast with CN37, which experiences a collapse in structure. The interfacial areas form a shell skin, and a hollow structure results because the internal CN structure from the $Ti(C_{0.3}N_{0.7})$ disappears owing to the formation of CNCl and C_xN_y gases.

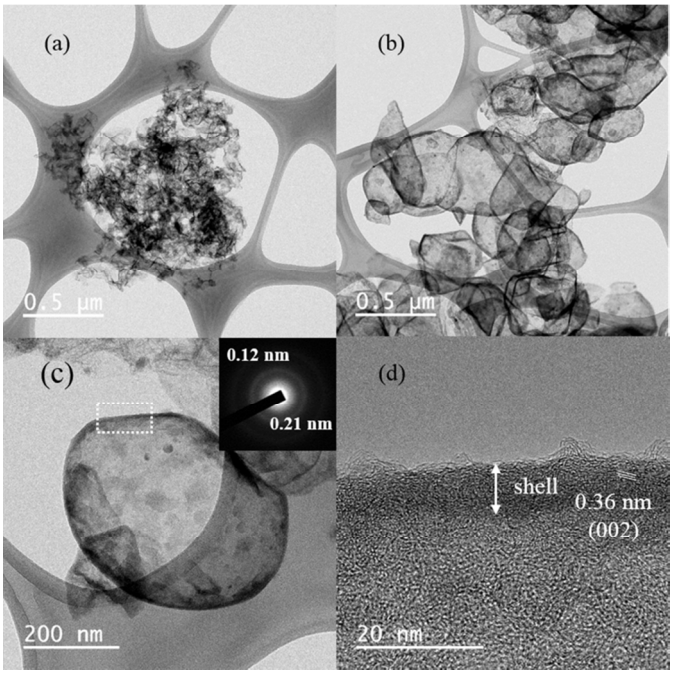

Figure 3. TEM images of CN37 (a), CNB37 (b),(c). HR-TEM image of CNB37(d) and corresponding SAED pattern (inset in (c)) at the shell area that marked in (c) as a rectangular dashed line.

The CNB hollow surface is stabilized not only by the direct interaction of boron with the surface layer but also by BCl_3 that is formed from the reaction between TiB_2 and Cl_2. BCl_3 is a strong Lewis acid, thus Lewis acid–base (nitrogen functional group) interaction induces a relatively lower exterior surface energy than that of the inner surface. This is similar to the hollow structure obtained from iron oxide by inorganic anions in solution.[35] As a result, the shell is formed and densification follows as the loosely-connected CNB shell gains part of the C–N moieties from the interior. This is well-supported by the fact that the size of the hollow structure in Figure 3(b) closely matches that of the precursor, $Ti(C_{0.3}N_{0.7})$ in Figure 2 (e), and that the mass of resultant CNB37 increases from 1.5% to 18.3% as listed in Table S1, compared with that of CN37. Thus, we conclude that the presence of boron in CN stabilizes the C–N bonding and facilitates the formation of a robust CNB hollow structure.

Elemental mapping of CNB37 (Figure 4(a) to (c)) shows that C, N, and B atoms are distributed uniformly without segregation. Strong mapping intensity along the granule boundaries in the figure is another evidence of the hollow structure.[34] The corresponding electron energy loss spectroscopy (EELS) spectrum is given in

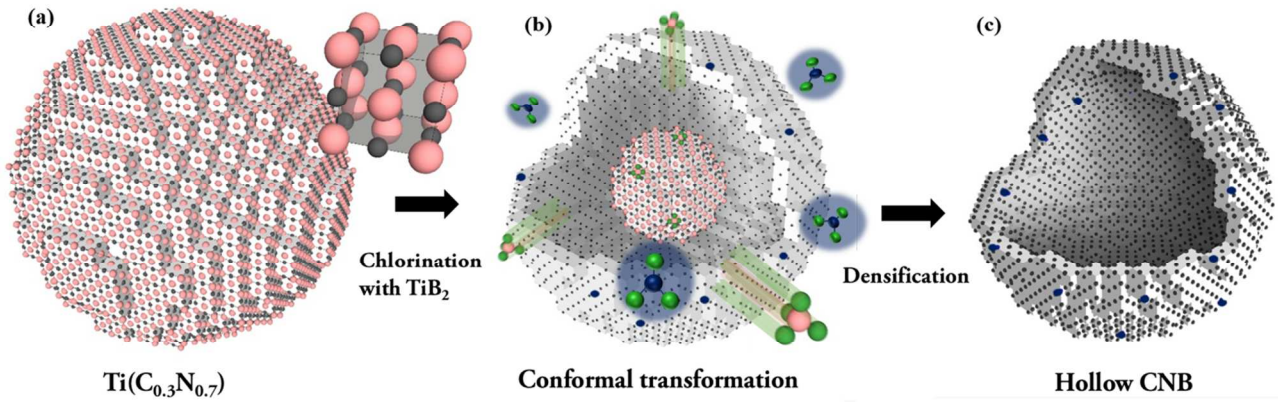

Scheme 1. Proposed mechanism of the formation of hollow CNB37 structure: (a) For simplicity, the $Ti(C_{0.3}N_{0.7})$ precursor is drawn to a sphere. The initial morphology is expected to be conformal to that of $Ti(C_{0.3}N_{0.7})$ after titanium extraction by chlorination, resulting in a porous structure. (b) CNB37 of high stability forms along the surfaces of the $Ti(C_{0.3}N_{0.7})$ particles, which is in contact with TiB_2 precursors and (c) a hollow structure results as the internal CN structure from the $Ti(C_{0.3}N_{0.7})$ precursor disappears by forming CNCl and C_xN_y gases. Each color indicates titanium (whitish red), carbon or nitrogen (black), boron (blue), and chlorine (green), respectively. The CNB37 quartered is omitted for the clarity.

Figure 4(d). The two high intensity peaks at ~284 eV and 292 eV are related to the 1s–π* and 1s–σ* transitions of the C K-shell excitation edges, respectively, which means that abundant graphitic carbon is present.[16] The sp^2 bonding character of the N atoms is shown by two broad peaks at approximately 400 eV.[36] Weak signals exist around

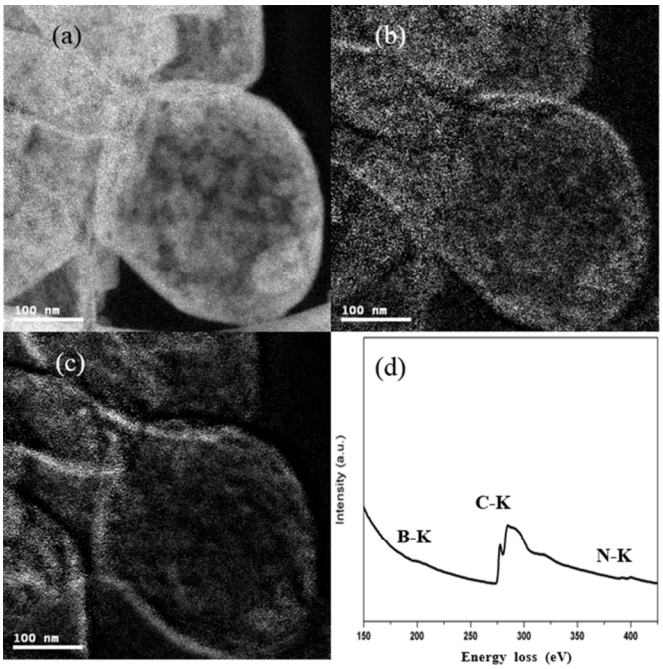

Figure 4. Elemental mapping of Carbon (a), Nitrogen (b), Boron (c) and EELS spectrum of CNB37 (d) in the same region.

194 eV. These originate from the B K-shell excitation edges and are attributed to the low boron content. These signals are more obvious when the content of boron precursor is increased as shown in Figure S3. Two distinguishable regions exist in Figure S3: one C rich and one BN rich. The latter exhibits two clear peaks in the region 190–195 eV. The lower peak (191 eV) originates from boron bonded to carbon, whereas the higher peak (194 eV) is caused by the binding of boron to nitrogen.[16]

To determine their accurate chemical composition and bonding nature, CNs and CNBs were analysed by X-ray photoelectron spectroscopy (XPS) (Table 1). Elemental analysis (EA) and inductively coupled plasma-atomic emission spectroscopy (ICP-AES) were used to determine the bulk compositions, which were compared with the surface compositions from XPS. According to Table 1, CNBs consist mostly of carbon, nitrogen, boron, and oxygen, with the amounts varying according to those of the precursor. An increase in nitrogen content in the bulk compared with the surface is observed in all samples, which is common for CNs.[37] The boron content in the CNBs increases on the surface and seems to be related to our proposed surface-preferred reaction.

No large difference exists among the samples in the nitrogen-bonding states as depicted in Figures 5 and S4. Although there is some difference in their relative amounts, pyridinic nitrogen (N_{pyr}) at

Table 1. Chemical composition of synthesized meterials measured by XPS. The values in the parentheses are for bulk compositions taken by EA analysis for N and ICP measurment for B, respectively. The ratio of nitrogen functional groups are evaluated by their areal integrations. The amount of CO_2 capture and CO_2/N_2 selectivities are measured at 298K . The CO_2 partial pressure of 0.1 bar is selected for the standard of the selectivity.

	C (wt%)	B (wt%)	O (wt%)	N (wt%)	Nitrogen functional groups			CO_2 capture (1 bar) (mmol/g)	CO_2/N_2 selectivity
					Pyridinic (398.2 eV, %)	Quaternary (400.8 eV, %)	Pyridine-N-oxide (402.8 eV, %)		
CNB73	84.6	1.4 (1.0)	7.3	4.5 (5.5)	49.4	47.7	2.9	3.10	16.6
CNB55	82.4	1.1 (0.7)	9.2	6.2 (8.0)	45.5	51.3	3.2	3.05	17.3
CNB37	79.9	0.4 (0.2)	10.1	8.2 (9.5)	44.8	50.5	4.7	3.70	35.2
CN73	88.3	0	7.2	2.2 (2.9)	35.3	64.7	0	2.55	16.4
CN55	85.4	0	9.0	3.8 (4.5)	28.1	71.9	0	2.33	16.8
CN37	77.6	0	14.2	6.5 (7.9)	37.1	54.7	8.2	-	-

398.2 eV and quaternary nitrogen (N_q) at 400.8 eV developed mostly in the CNs and CNBs during the chlorination 800°C. At that temperature, normal nitrogen functional groups usually change to N_q as observed in another study.[6] However, $TiCl_4$, which facilitates pore formation during CN or CNB synthesis, is presumed to promote the formation of N_{pyr} in the system.

Given that the binding energy of N_{pyr} is similar to that of the B–N moiety in the N 1s XPS spectrum, it is difficult to distinguish them from one another in our CNBs. Therefore, the B 1s XPS spectrum was deconvoluted. The results shown in Figure S5 indicate that C–B–N and B–N bonding (190.9 eV) are the main sources of boron interaction. However, a small BC_3 contribution also appears as a sub-peak (189 eV), and this peak increases as the nitrogen content in the precursors increases. Even though BC_3 bonds are formed, they are unstable and break easily. However, once boron is bound to carbon, it stabilizes the reaction, and strengthens the C–N bonds. Despite its low boron content, the high nitrogen content of CNB37 proves that this nitrogen increment is not ascribed to that from B–N bonding. It seems that the role of BC_3 is more vigorous in strengthening the C–N bond under nitrogen-rich conditions.

First principle calculations were performed to understand the effect of BC_3 on the nitrogen functional groups. For convenience of calculation, the quaternary nitrogen, the most abundant functional group, was built into the graphene structure and evaluated in terms of stability. The formation energy E_{form} of each nitrogen functional group is calculated as follows:

$$E_{form} = E_{total}\text{ (N-doped graphene) - }E_{total}\text{ (graphene)} + \mu_C - \mu_N \quad (1)$$

$$E_{form} = E_{total}\text{ (B- and N-co-doped graphene) - }E_{total}\text{ (B-doped graphene)} + \mu_C - \mu_N, \quad (2)$$

where E_{total} is the total energy of the system, and μ_x is the chemical potential of element x. A negative value of E_{form} indicates a spontaneous reaction and vice versa. Boron has one fewer valence electron than carbon, while nitrogen has one more. Therefore, a structure-stabilizing charge compensation is expected from their co-doping. The calculation shows that the most stable configuration is formed when nitrogen is connected directly to boron as shown in Figure 6. The reduction in the formation energy is always lower

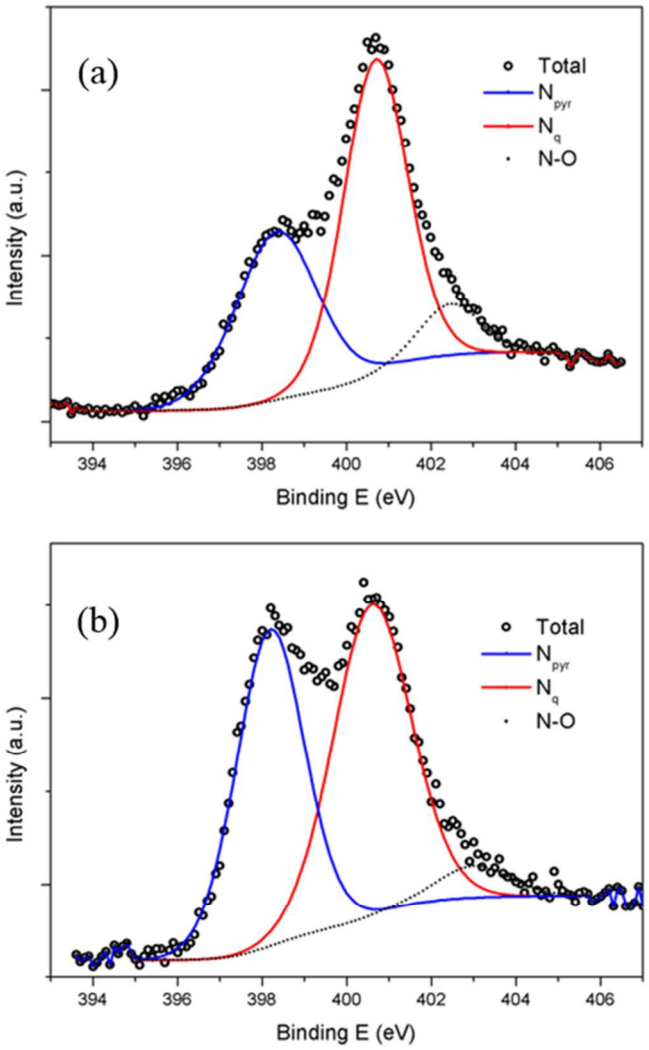

Figure 5. XPS N 1s spectra of CN37 (a) and CNB37 (b). Each peaks are deconvoluted into several functional groups as N_{pyr} (398.2 eV), N_q (400.8 eV) and N-O (402.8 eV).

when boron is close to nitrogen than in the case without boron. This means that nitrogen is more available to bond effectively with carbon in the presence of boron. A similar stabilization effect is also noted for BCl_3 addition as shown in Figure S6. This proves that with the addition of boron, its intermediate phase can act as a stabilizing agent for nitrogen incorporation. Other boron compounds, as well as BCl_3, are expected to behave in a similar way owing to their common Lewis acid properties.

CO_2 adsorption by the nitrogenous porous carbons were studied to evaluate their potential for carbon capture (Figure 7(a)). A summary of these capture properties for the CNs and CNBs is given in Table 1. The quantity of CN37 obtained is small (see the yield in Table S1) and unreliable, thus this result is excluded. Every CNB provides a

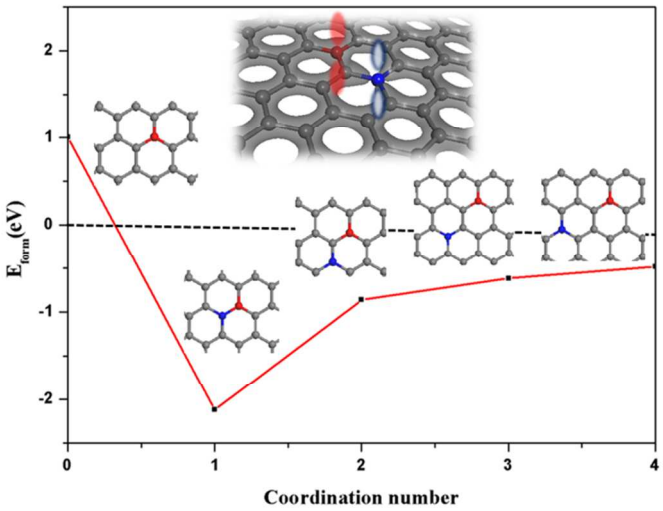

Figure 6. Calculated formation energy of Nitrogen doping in graphene sheet with respect to the B position relative to N. Carbon (gray), nitrogen (red) and boron (blue) atoms are indicated in colors.

better uptake than the corresponding CN regardless of surface area. A noticeable uptake of 3.7 mmol/g is achieved by CNB37. No degradation was observed after five repeated cycles of CO_2 capture measurements without any heat treatment (Figure S7). The CO_2/N_2 selectivity, extrapolated on the basis of ideal adsorption solution theory (IAST),[38] increases significantly for CNB37 (Figure 7(b)). An outstanding selectivity of 35.2 was observed at a CO_2 partial pressure of 0.1bar and a total pressure of 1bar (these conditions are similar to those of a real post-combustion gas mixture). This selectivity is better than the best reported for a CN material.[10]

This selective sorption by a non-ordered structure is usually explained by the presence of nitrogen atoms on the pore surface, which can increase the surface–adsorbate interaction.[39] In our experiments, the selectivity increases with nitrogen content, especially at low CO_2 partial pressure. However, when comparing the selectivity difference between CNB73 and CNB55, the significant increase for CNB37 cannot be explained simply by the nitrogen content or character of the functional groups. The uniqueness of the hollow CNB37 in terms of its short pore features and hierarchical structure could be the reason for its enhanced ability to capture large quantities of CO_2 and its improved selectivity. The effect of morphology on carbon capture and storage area has not yet been well discussed, but a hollow structure has demonstrated outstanding properties in various fields such as gas sensors and catalysts.[40, 41] A significant increase in hydrogen uptake by hollow BN has also been reported.[34] The robustness of shell was obtained by eliminating a washing step with a strong acid, which is essential in

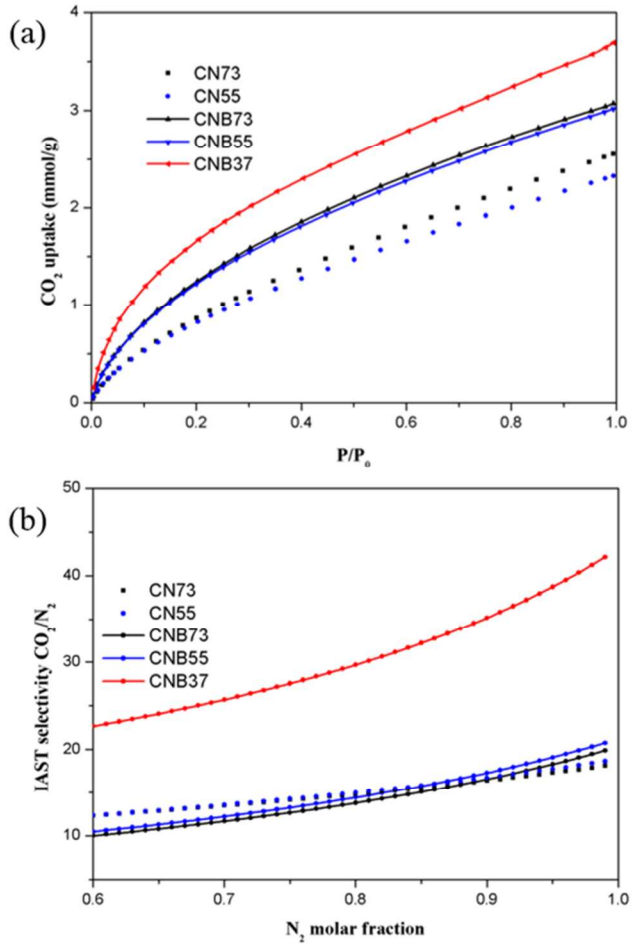

Figure 7. CO_2 adsorption isotherms of CNs and CNBs measured at 298K (a) and their CO_2/N_2 selectivity versus N_2 molar fraction (b) at total pressure of 1 bar evaluated by IAST method.

template method, resulting in the enhancement compared to reported nitrogenous hollow carbon.[23] Therefore, it is worth noting that the hollow structure of template-free CNB37 is effective in CO_2 capture and CO_2/N_2 selectivity.

Conclusions

Nitrogen-containing porous carbons with a large surface area were prepared by the addition of boron during synthesis at high temperature. The addition of a small amount of boron changes the reaction atmosphere and facilitates the introduction of nitrogen into the carbon structure. The CNBs obtained from the chlorination process show a higher thermal stability and productivity (yield) than the corresponding CNs. Among the CNBs, CNB37 has a hollow granule structure. The nitrogen-rich titanium carbo-nitride precursor is self-templating. During the reaction titanium is consumed, and a hollow shell structure remains. The mechanism can be explained as the direct doping of boron at the surface of the precursor particles along with a loss of interior CN and the effect of BCl_3 in a Lewis acid–base interaction. It is worth noting that a morphological modification of CN or CNB would be possible, depending on the shape control of the nitrogen-containing precursor without any post-treatment. Although CNB37 possesses the smallest area of the fabricated structures, it shows the highest CO_2 uptake and CO_2/N_2 selectivity at ambient temperature. Its hollow morphology appears to enhance the sensitivity of the interaction. Additional work for further improvement and the development of various applications, based on a self-templating hollow CNB, are now in progress and will be discussed in our future publications.

Acknowledgements

This research was supported partially by Hanwha Chemical, Korea and partially by BK PLUS through the Korea Ministry of Education, Science and Technology. The authors acknowledge the use of the services and facilities at the Research Institute of Advanced Materials, Seoul National University. We are also thankful to Dr. Y.-S. Kim at the Korea Basic Science Institute for supporting our work on the calculation tools with helpful discussions.

Notes and references

Department of Materials Science and Engineering, Seoul National University, Seoul, 151-742, Korea. E-mail: Shinkang@snu.ac.kr

Electronic Supplementary Information (ESI) available: TEM images of porous CNBs, XRD pattern, EELS spectra, XPS N 1s spectra, XPS B 1s spectra, Geometric configuration of BCl_3 with nitrogen doped graphene sheet, Cycle test of CO_2 capture for CNB37, textural properties of fabricated materials and IAST calculation method. See DOI: 10.1039/b000000x/

1. J. Lee, J. Kim and T. Hyeon, Adv. Mater., 2006, 18, 2073-2094.
2. P. Simon and Y. Gogotsi, Nat. Mater., 2008, 7, 845-854.
3. C. D. Liang, Z. J. Li and S. Dai, Angew. Chem.-Int. Edit., 2008, 47, 3696-3717.
4. X. H. Li and M. Antonietti, Chem. Soc. Rev., 2013, 42, 6593-6604.
5. J. P. Paraknowitsch and A. Thomas, Energy Environ. Sci., 2013, 6, 2839-2855.
6. R. Arrigo, M. Havecker, R. Schlogl and D. S. Su, Chem. Commun., 2008, 4891-4893.

7. G. P. Hao, W. C. Li, D. Qian and A. H. Lu, Adv. Mater., 2010, 22, 853-857.
8. C. Pevida, T. C. Drage and C. E. Snape, Carbon, 2008, 46, 1464-1474.
9. Y. D. Xia, R. Mokaya, G. S. Walker and Y. Q. Zhu, Adv. Energy Mater., 2011, 1, 678-683.
10. Y. F. Zhao, X. Liu, K. X. Yao, L. Zhao and Y. Han, Chem. Mat., 2012, 24, 4725-4734.
11. T. C. M. Chung, Y. Jeong, Q. Chen, A. Kleinhammes and Y. Wu, J. Am. Chem. Soc., 2008, 130, 6668-6669.
12. Z. H. Sheng, H. L. Gao, W. J. Bao, F. B. Wang and X. H. Xia, J. Mater. Chem., 2012, 22, 390-395.
13. W. Lei, D. Portehault, R. Dimova and M. Antoniettit, J. Am. Chem. Soc., 2011, 133, 7121-7127.
14. S. Y. Wang, E. Iyyamperumal, A. Roy, Y. H. Xue, D. S. Yu and L. M. Dai, Angew. Chem.-Int. Edit., 2011, 50, 11756-11760.
15. X. H. Li and M. Antonietti, Angew. Chem.-Int. Edit., 2013, 52, 4572-4576.
16. E. Iyyamperumal, S. Y. Wang and L. M. Dai, ACS Nano, 2012, 6, 5259-5265.
17. H. L. Guo and Q. M. Gao, J. Power Sources, 2009, 186, 551-556.
18. D. Portehault, C. Giordano, C. Gervais, I. Senkovska, S. Kaskel, C. Sanchez and M. Antonietti, Adv. Funct. Mater., 2010, 20, 1827-1833.
19. T. Komatsu and A. Goto, J. Mater. Chem., 2002, 12, 1288-1293.
20. J. Kim, J. Han, M. Seo, S. Kang, D. Kim and J. Ihm, J. Mater. Chem. A, 2013, 1, 1014-1017.
21. V. Presser, M. Heon and Y. Gogotsi, Adv. Funct. Mater., 2011, 21, 810-833.
22. J. H. Jiang, Q. M. Gao, Z. J. Zheng, K. S. Xia and J. Hu, Int. J. Hydrog. Energy, 2010, 35, 210-216.
23. S. S. Feng, W. Li, Q. Shi, Y. H. Li, J. C. Chen, Y. Ling, A. M. Asiri and D. Y. Zhao, Chem. Commun., 2014, 50, 329-331.
24. J. L. Zimmerman, R. Williams, V. N. Khabashesku and J. L. Margrave, Nano Lett., 2001, 1, 731-734.
25. Y. S. Jun, E. Z. Lee, X. C. Wang, W. H. Hong, G. D. Stucky and A. Thomas, Adv. Funct. Mater., 2013, 23, 3661-3667.
26. X. W. Lou, L. A. Archer and Z. C. Yang, Adv. Mater., 2008, 20, 3987-4019.
27. J. Hu, M. Chen, X. S. Fang and L. W. Wu, Chem. Soc. Rev., 2011, 40, 5472-5491.
28. D. M. D'Alessandro, B. Smit and J. R. Long, Angew. Chem.-Int. Edit., 2010, 49, 6058-6082.
29. A. Samanta, A. Zhao, G. K. H. Shimizu, P. Sarkar and R. Gupta, Ind. Eng. Chem. Res., 2012, 51, 1438-1463.
30. M. S. Seo, J. H. Kim, J. M. Kim, J. S. Han, S. Kang, J. S. Ihm and D. O. Kim, Carbon, 2013, 60, 299-306.
31. G. Yushin, R. Dash, J. Jagiello, J. E. Fischer and Y. Gogotsi, Adv. Funct. Mater., 2006, 16, 2288-2293.
32. F. D. Han, Y. J. Bai, R. Liu, B. Yao, Y. X. Qi, N. Lun and J. X. Zhang, Adv. Energy Mater., 2011, 1, 798-801.
33. C. W. Wang, Y. Wang, J. Graser, R. Zhao, F. Gao and M. J. O'Connell, ACS Nano, 2013, 7, 11156-11165.
34. G. Lian, X. Zhang, S. J. Zhang, D. Liu, D. L. Cui and Q. L. Wang, Energy Environ. Sci., 2012, 5, 7072-7080.
35. C. J. Jia, L. D. Sun, Z. G. Yan, L. P. You, F. Luo, X. D. Han, Y. C. Pang, Z. Zhang and C. H. Yan, Angew. Chem.-Int. Edit., 2005, 44, 4328-4333.
36. A. Vinu, M. Terrones, D. Golberg, S. Hishita, K. Ariga and T. Mori, Chem. Mat., 2005, 17, 5887-5890.
37. T. P. Fellinger, F. Hasche, P. Strasser and M. Antonietti, J. Am. Chem. Soc., 2012, 134, 4072-4075.
38. A. L. Myers and J. M. Prausnitz, Aiche J., 1965, 11, 121-127.
39. J. R. Li, R. J. Kuppler and H. C. Zhou, Chem. Soc. Rev., 2009, 38, 1477-1504.
40. C. Song, J. P. Du, J. H. Zhao, S. A. Feng, G. X. Du and Z. P. Zhu, Chem. Mat., 2009, 21, 1524-1530.
41. J. H. Lee, Sens. Actuator B-Chem., 2009, 140, 319-336.